Water oxidation catalysis on the nitrogen-deficient $SrNbO_2N$ (001) surface

Vasyl Stotskyi and Ulrich Aschauer*

Department of Chemistry and Biochemistry, University of Bern, Freiestrasse 3, Bern, CH–3012, Switzerland

E-mail: ulrich.aschauer@dcb.unibe.ch

Abstract

Perovskite oxynitrides are a promising class of photocatalysts to drive the oxygen evolution (OER) half-reaction of water splitting. They are however known to be less stable than pure oxides and may lose nitrogen, in particular in the early stages of their operation. Under OER conditions, nitrogen vacancies are likely to be filled with oxygen, thus altering the stoichiometry of the surface. Here we investigate, using density functional theory calculations, the effect of this substitution on the surface electronic structure and catalytic activity under OER conditions. We show that the investigated oxynitride $SrNbO_2N$, due to the multivalent nature of the Nb cations, behaves differently than the related $SrTaO_2N$. In particular, we show that under OER conditions, the substitution of N by O does enhance the reactivity, which is optimal around $^3/_4$ substitution, given the ideal balance of excess charge injection and the suppression of O-N dimer formation. These results highlight the rich surface chemistry of oxynitrides, which strongly depends on the surface stoichiometry that represents a potential tuning knob for the activity of these materials.

Introduction

Solar radiation is an abundant, renewable form of energy that, if converted efficiently to electrical or chemical energy, could more than cover humanity's energy requirements[1]. One issue with solar energy is its unavailability at night or when the sun does not shine, requiring energy storage, typically as either potential energy such as in pump storage dams or chemical energy such as in batteries or fuels[2]. Given its transportability, chemical energy, is better suited for mobility applications, fuels having the further advantage of much faster refueling times compared to battery recharging. These fuels can either be directly combusted or with the help of fuel cells converted to electricity when needed. Hydrogen (H_2) as a fuel is particularly appealing as the combustion/conversion would result in only water as the byproduct[3]. While photovoltaic conversion of solar energy to electricity combined with an

electrolyzer to split water into O_2 and the H_2 fuel relies on relatively mature and efficient technology, the two-step conversion will necessarily lead to less than ideal efficiencies. The single-step photocatalytic conversion of water to H_2 and O_2 has hence attracted significant interest since its discovery almost half a century ago[4].

Despite its appeal, the direct conversion of solar energy to chemical fuels is hampered by the availability of suitable catalysts to drive the reaction[5]. The catalyst material needs to be able to absorb a large fraction of the solar spectrum, limiting the choice to semiconductor materials. For water splitting, the band gap has to be larger than the minimum energy of 1.23 eV required to split one water molecule (in practice larger band gaps are required to provide sufficient overpotential) but also has to be smaller than about 2.5 eV to absorb a significant fraction of the solar spectrum. Moreover, the materials need to have band edges aligned to allow electron or hole transfer to the reduction and oxidation reactions respectively, they need to be stable under application conditions and have sufficient carrier mobilities for efficient separation of photo-excited electrons and holes. Despite a lot of research, a material that ideally combines all these properties has not yet been found.

The overall water-splitting reaction

$$2\,H_2O \rightarrow 2\,H_2 + O_2 \tag{1}$$

can be divided in two half reactions, the oxygen evolution reaction (OER)

$$2\,H_2O + 4\,h^+ \rightarrow O_2 + 4\,H^+ \tag{2}$$

and the hydrogen evolution reaction (HER)

$$4\,H^+ + 4\,e^- \rightarrow 2\,H_2. \tag{3}$$

Of these reactions the OER is known to have sluggish kinetics, making it the bottleneck

in the overall reaction. The catalyzed OER is commonly assumed to proceed by four individual proton-coupled-electron transfer (PCET) steps, labeled A-D (see Figure 1), where * represents an active site on the surface:

$$\mathrm{A}: \quad * + \mathrm{H_2O} \quad \rightarrow \quad *\mathrm{OH} + \mathrm{H^+} + \mathrm{e^-} \tag{4}$$

$$\mathrm{B}: \quad * \mathrm{OH} \quad \rightarrow \quad *\mathrm{O} + \mathrm{H^+} + \mathrm{e^-} \tag{5}$$

$$\mathrm{C}: \quad * \mathrm{O} + \mathrm{H_2O} \rightarrow *\mathrm{OOH} + \mathrm{H^+} + \mathrm{e^-} \tag{6}$$

$$\mathrm{D}: \quad * \mathrm{OOH} \quad \rightarrow * + \mathrm{O_2} + \mathrm{H^+} + \mathrm{e^-} \tag{7}$$

While alternative mechanisms involving lattice oxygen were reported to potentially yield higher activities[6–8], especially for materials with easy oxygen-vacancy formation, this mechanism usually represent a good starting to point to computationally evaluate the activity of a given OER catalyst[9,10].

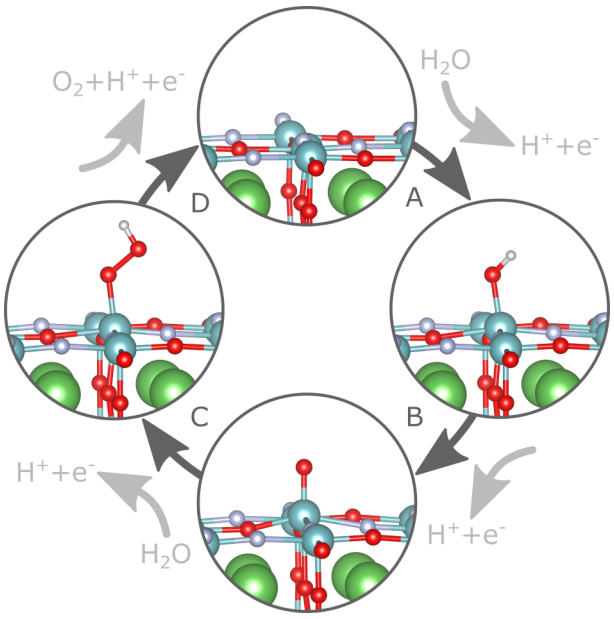

Figure 1: OER mechanism on the clean and stoichiometric $SrNbO_2N$ surface involving the *OH, *O and *OOH reaction intermediates, which are shown in their relaxed geometry.

One particularly appealing class of materials to search for stable photocatalytic water-splitting materials is the perovskite structure with the general formula ABX_3. This structure

displays a large chemical freedom as many elements can be accommodated on the cationic A and B as well as the anionic X sites. Oxides (X=O) are the most studied perovskites but typically have too large band gaps to absorb visible light ($NaTaO_3$: 4.1 eV, $KTaO_3$: 3.6 eV)[11,12]. Oxynitrides, with both O and N on the X site, on the other hand, show reduced band gaps ($SrTaO_2N$: 2.1 eV) due to the lesser electronegativity of N compared to O[13]. Oxynitride photocatalysts that absorb in the visible range were first investigated in 2002[14] and since then mainly titanate and tantalate perovskite oxynitrides have been studied[13,15–17]. While the bulk structure and properties of these materials are now fairly well understood[18], their surfaces that actually catalyze the redox reactions were studied much less.

In the present work we investigate, using density functional theory calculations, the surface chemistry of the niobate perovskite oxynitride $SrNbO_2N$. Compared to the previously investigated tantalates, niobates are more easily reduced from the usual 5+ B-site oxidation state to 4+, which is expected to have an effect on the excess-charge accommodation and hence the surface chemistry. We study the dominant (001) surface and consider the spontaneous substitution of N by O in the surface layer under photocatalytic conditions that was reported for $SrTaO_2N$[19]. We then compute the OER on these substituted surfaces, also investigating the effect of the thermodynamically stable adsorbate structure determined via computed surface Pourbaix diagrams. Our results show that defect formation and hence substitution of N by O is significantly easier on $SrNbO_2N$ compared to $SrTaO_2N$, which we can relate to the multivalent nature and hence easier reduction of Nb compared to Ta. The multivalent nature also leads to an unequal distribution of excess electrons over surface Nb sites that can affect the binding of intermediate species. Under conditions relevant for the OER, we obtain the highest OER activity when 3/4 of the surface N atoms are replaced by O atoms, since the number of highly stable O-N dimer species is reduced. These results show that nitrogen loss is not necessarily detrimental to the OER activity of perovskite oxynitrides but depends on the surface adsorbate structure.

Methods

All density functional theory (DFT) calculations were carried out with the QUANTUM ESPRESSO package[20,21] using the Perdew-Burke-Ernzerhof (PBE) exchange correlation functional[22]. As shown in the supporting information Fig. S1, the effect of a DFT+U correction on the electronic structure is minimal, as expected for fairly diffuse Nb 4d orbitals and we therefore perform calculations without this correction. Ultrasoft pseudopotentials[23] with Sr(4p, 5s), Nb(5s, 4d), O(2s, 2p) and N(2s, 2p) valence states were used to describe electron-nuclear interactions and wave functions were expanded in plane waves up to a kinetic energy cutoff of 40 Ry combined with 320 Ry for the augmented density.

Internal coordinates and cell parameters of $SrNbO_2N$ bulk structures were relaxed in different space groups in 20-atom unit cells using $6 \times 6 \times 4$ k-meshes[24]. For the lowest energy bulk structure we performed an HSE06[25,26] calculation based on the PBE structure to obtain an accurate band gap. The most stable of these cells was subsequently transformed into a 40-atom cell for slab construction. The {001} surface orientation is known to be most stable in perovskite oxides and oxynitrides[27,28] and we consider here the catalytically active transition-metal BO_2 termination. An eight atomic layer thick (001) slab (lateral dimensions 8.2516×8.2516 Å) was constructed from this relaxed structure, using a 15 Å vacuum gap to separate periodic images along the surface normal direction along with a dipole correction[29]. Reciprocal space for these slab calculations was sampled using a $4\times4\times1$ k-point mesh. Relaxation thresholds were set to 10^{-6} Ry and 10^{-3} Ry/bohr for the total energy and forces respectively in all calculations.

The surface-adsorbate structure as a function of the experimental conditions (pH and potential U_b) was determined via surface Pourbaix diagrams for which the stability of a fully O- and OH-covered surface relative to the clean surface was evaluated within the computational hydrogen electrode (CHE) approach[9,10]:

$$\Delta G = \Delta E + (\Delta \mathrm{ZPE} - T\Delta S) - eU_b - k_B T \ln(10)\mathrm{pH}. \tag{8}$$

Here ΔE is the DFT total energy difference between the clean and adsorbate covered surface, ΔZPE and $T\Delta S$ account for zero-point energy and entropy changes associated with the adsorbates and the terms with U_b and pH consider the transfer of electrons and protons to a reservoir (one electron and proton per OH and two electrons and protons per O adsorbate). Since the ZPE terms show a negligible material and site dependence, they were taken from previous work[10], while the entropy considers only vibrational terms in gas phase that were taken from standard tables[30].

The free energy profile of the OER according to the four-step mechanism given by equations 4-7 was also evaluated within the above thermochemical approach by computing the DFT total energy differences between the *, *OH, *O and *OOH reaction intermediates (see Figure 1) and assuming transfer of one electron and proton to their respective reservoirs in each reaction step i. Based on these four reaction free energies, the thermodynamic overpotential η, is defined as the difference between the highest reaction step per electron and the OER equilibrium potential (1.23 V at pH = 0):

$$\eta = \frac{\max(\Delta G_i)}{e} - 1.23. \tag{9}$$

Even though experiments are typically conduced under alkaline conditions, this overpotential is meaningful as the pH dependence of both ΔG and the equilibrium potential renders the thermodynamic overpotential pH independent[31]. All overpotentials were calculated without considering the effect of either an explicit or implicit solvent that could lead to a slight stabilization of the reaction intermediates and hence a slightly lower overpotential[32].

Results and discussion

We find the most stable $SrNbO_2N$ bulk structure (Fig. 2a) to have the orthorhombic $Pmn2_1$ space group. This structure differs from X-ray and neutron diffraction studies[33,34] that reported the tetragonal I4/mcm space group. This discrepancy is likely related to the

most-stable explicit *cis* nitrogen order in the *ab* plane used in our 0K DFT calculations, whereas experiments at finite temperature show no such long-range anion order. This finding of the lowest energy structure is, however, in agreement with the one found in DFT calculations of the tantalate perovskite oxynitride $SrTaO_2N$[35] and the general preference for *cis* compared to *trans* anion order in perovskite oxynitrides[36,37].

For this lowest energy structure, we compute an HSE06 band gap of E_{gap} of 2.80 eV. Using this band gap for an empirical estimation[38–40] of the band edges based on the position of the normal hydrogen electrode (NHE) with respect to the vacuum level $E_0 = -4.5$ eV and the Mulliken electronegativities χ of the various elements

$$E_{\mathrm{VB,CB}} = E_0 + (\chi_{\mathrm{Sr}}\chi_{\mathrm{Nb}}\chi_{\mathrm{O}}^2\chi_{\mathrm{N}})^{1/5} \pm E_{\mathrm{gap}}/2, \tag{10}$$

we obtain valence (VB) and conduction band (CB) edges at 2.29 and -0.51 eV respectively vs. NHE. These band edges below and above the water oxidation (1.23 eV) and hydrogen reduction (0.00 eV) potentials imply that $SrNbO_2N$ is suitable to drive overall water splitting.

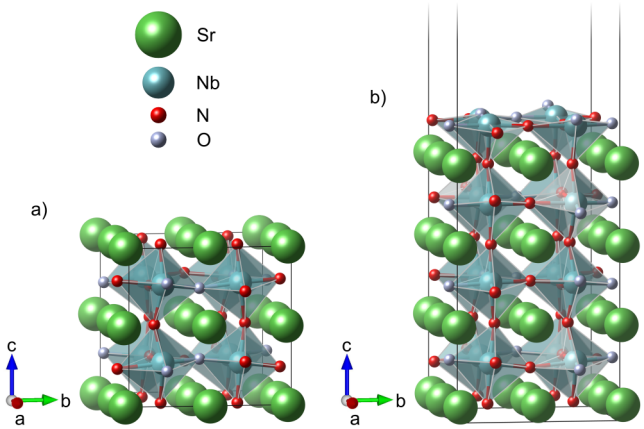

Figure 2: Crystal structures of (a) the lowest energy $SrNbO_2N$ bulk structure with a *cis* N anion order in the *ab*-plane and (b) the corresponding (001) surface slab.

Our results differ from $SrTaO_2N$ in the sense that anion vacancy formation and the concomitant reduction of the cation sublattice is much easier in $SrNbO_2N$. This is shown in Table 1 that reports the concentration-dependent formation energy of vacancies on site i

(i=O, N)

$$\Delta E_{\mathrm{form},i} = (E_{\mathrm{def},n_i} + n_i\mu_i - E_{\mathrm{stoi}})/n_i \tag{11}$$

for the most oxygen and nitrogen-rich conditions (μ_i) compatible with $SrNbO_2N$ phase stability evaluated via the CPLAP code[41]. In this equation E_{def,n_i} is the total energy of a cell containing n_i vacancies on site i and E_{stoi} is the total energy of the stoichiometric cell. We focus here on neutral defects only, differently charged defects being an interesting topic for further study. While V_O have a much reduced formation energy compared to the bulk-like region in $SrTaO_2N$[19] (using the same approach as above, we recomputed bulk formation energies of around 3.5-3.7 eV for V_O and 3.5 eV for V_N in $SrTaO_2N$) the V_N formation energy in $SrNbO_2N$ is negative showing that $SrNbO_2N$ will spontaneously reduce by formation of nitrogen vacancies. We can however see that due to vacancy-vacancy interaction, the formation energy of two or more nitrogen vacancies is no longer negative. This implies that $SrNbO_2N$ will spontaneously be reduced and adopt a nitrogen deficiency between $^1/_8$ and $^2/_8$. This easier reduction can be explained by the multivalent (Nb_5^+/Nb_4^+) nature of Nb which is not the case for Ta and results in the easier accommodation of excess electrons during reductive anion vacancy formation.

Table 1: Anion vacancy formation energy in bulk $SrNbO_2N$. For V_O we distinguish vacancies lying within the *cis* N plane and perpendicular to it.

Defect	Position	n_i	ΔE_{form} (eV)
V_O	in-plane	1	1.33
	out-of-plane	1	1.49
V_N		1	-0.95
		2	1.12
		3	1.73

Based on the stoichiometric bulk structure, we constructed the stoichiometric, asymmetric slab model shown in Fig. 2b. We had previously shown that nitrogen in the surface layer of the perovskite oxynitride $SrTaO_2N$ has a tendency to be replaced with oxygen under OER conditions[19]. In $SrTaO_2N$ this substitution leads to an electron doping that, with

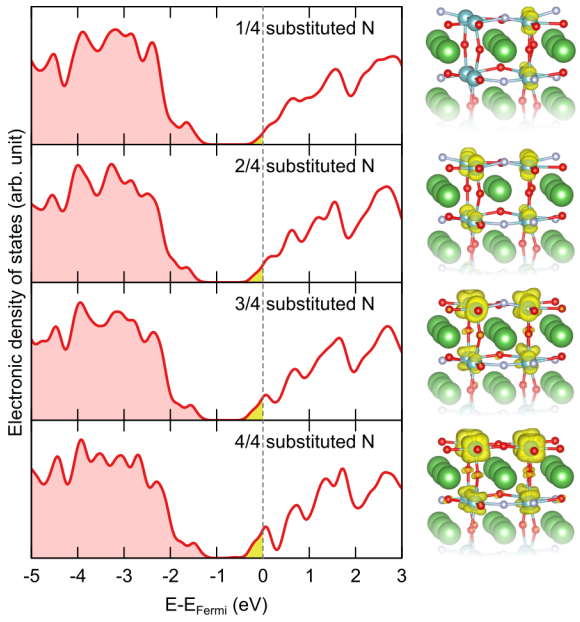

Figure 3: Total density of states as a function of the number of surface N substituted by O atoms. The yellow shaded area between the conduction-band edge and the Fermi level corresponds to the excess electrons resulting from this substitution. The isosurfaces ($3 \cdot 10^{-3}$ e/Å^3) show the localization of this charge at the $SrNbO_2N$ (001) surface.

increasing substitution fraction, localizes on the surface transition-metal d states, however remaining delocalized over all surface sites. Given the multivalent nature of Nb compared to Ta, one could expect that $SrNbO_2N$ could show polaron formation and hence localization of the excess electrons on individual Nb surface sites. We sampled all symmetry-inequivalent O substitutions of one, two, three and four out of the four surface N species on the stoichiometric surface, focusing in the following on the lowest energy geometry at each substitution level. We note that in the densities of states in Fig. 3 the band gap and the band edges are only minimally affected by the substitution. This is expected since the substitution is restricted to the very surface and the band edges remain dominated by the higher-lying nitrogen states in bulk layers. As such the band-edge positions remain suitable to drive the OER upon substitution. Indeed, we find for $^1/_4$ substitution that the excess charge density localizes primarily on the two Nb sites on the right in Fig. 3. When half of the N are substituted by O, this asymmetry in charge localization is less pronounced but clearly re-emerges for

the ¾ substitution level, where the two Nb sites at the back carry a larger fraction of the excess charge density. At full substitution the localization is again similar on all Nb sites. While this localization of charge could be linked to the ligands surrounding the Nb sites, it is in stark contrast to what was observed for $SrTaO_2N$ (see Fig. 4), which hints that the easier reduction of Nb compared to Ta is a likely explanation for this difference. Another difference with respect to $SrTaO_2N$ is that the charge does not fully localize at the surface but also on subsurface sites (see Fig. 3). Nevertheless one could expect the different electron density at different surface sites to affect the catalytic activity, which we will investigate in the following.

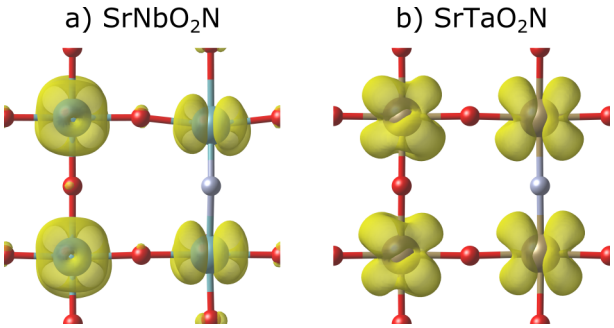

Figure 4: Excess charge localization at ¾ substitution on the (001) surface of a) $SrNbO_2N$ and b) $SrTaO_2N$, showing the asymmetric arrangement on the former and the symmetric arrangement on the latter.

To determine the thermodynamically most stable state of the surface, we next compute surface Pourbaix diagrams for surfaces with between zero and all four surface N atoms substituted with O. The Pourbaix diagrams shown in Fig. 5 show a clear trend for the shift of the onset potential for formation of an OH layer on the surface. As substitution and hence the reduction of the surface increases, the OH layer forms at increasingly lower potentials, already for two substituted N being clearly below zero, indicating a spontaneous hydroxylation of the surface without applied potential or light irradiation. The trend for the boundary between the OH and O covered surface is less clear: after an initial increase, we see it decreasing and finally sharply increase again. We associate this with the structural peculiarity of the oxygen adsorbate layer on the surface. Oxygen adsorbates have a tendency

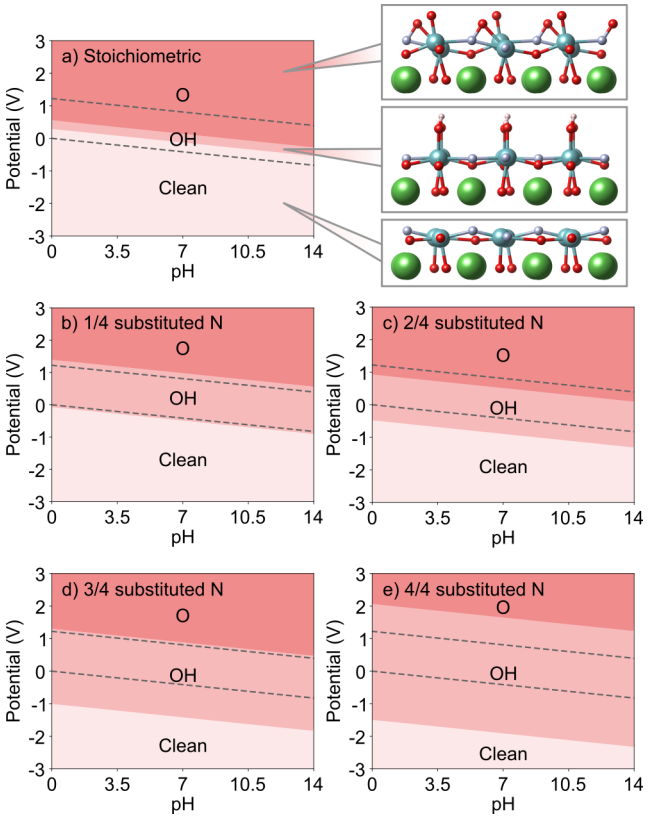

Figure 5: Calculated surface Pourbaix diagrams for (001) surfaces with different levels of substitution of N by O in the surface layer: a) stoichiometric surface with 4 N as well as b) 1/4, c) 2/4, d) 3/4 and e) 4/4 substituted N.

to lean towards surface N atoms, forming very stable O-N dimer structures, the dimers carrying a negative charge[42]. While such negatively charged dimers would be more easily formed with increasing N substitution, the substitution also reduces the number of O-N dimers than can form. As such there are two counteracting trends leading to the observed behavior.

Table 2: Overpotential determining step (ODS) and overpotential (η) of the most reactive site as a function of the number of substituted N atoms on a surface without additional adsorbates. The ODS letter corresponds to the transition between intermediates given by equations 4-7.

Substituted surface N	ODS	η (V)
0/4	C	0.985
1/4	C	0.925
2/4	C	2.089
3/4	C	2.365
4/4	C	2.691

Next we calculate the OER on surface slabs with different levels of substitution of N by O. In analogy to what was previously done for $SrTaO_2N$, this analysis is initially carried out on a clean surface without additional adsorbates following the reaction intermediate sequence $* \rightarrow *OH \rightarrow *O \rightarrow *OOH \rightarrow *$ as shown in equations 4-7. As shown in Table 2, we find that step C, the formation of *OOH given by equation 6 is highest and determines the overpotential for any surface nitrogen content. We also see that while the overpotential on a surface with one N substituted by O is nearly the same as on the stoichiometric surface, the overpotential sharply increases for two substituted N after which point only a small increase is observed for even higher substitution levels. We note that Table 2 reports only the overpotential of the most reactive site at each substitution level, while in Fig. 6 we show the spread of values at inequivalent sites. We have seen above that with increasing substitution level selected Nb surface atoms change their oxidation state from Nb^{5+} to Nb^{4+}. The observed trend in overpotential can therefore be explained with a stronger adsorbate binding at electron-rich Nb^{4+} sites, in particular of the O intermediates[19], which leads to the observed overall increase in overpotential as shown in Fig. 6b and c. The spread in

overpotentials for different Nb sites is due to the different oxidation states, sites that have a stronger Nb^{5+} character generally being more active for the OER.

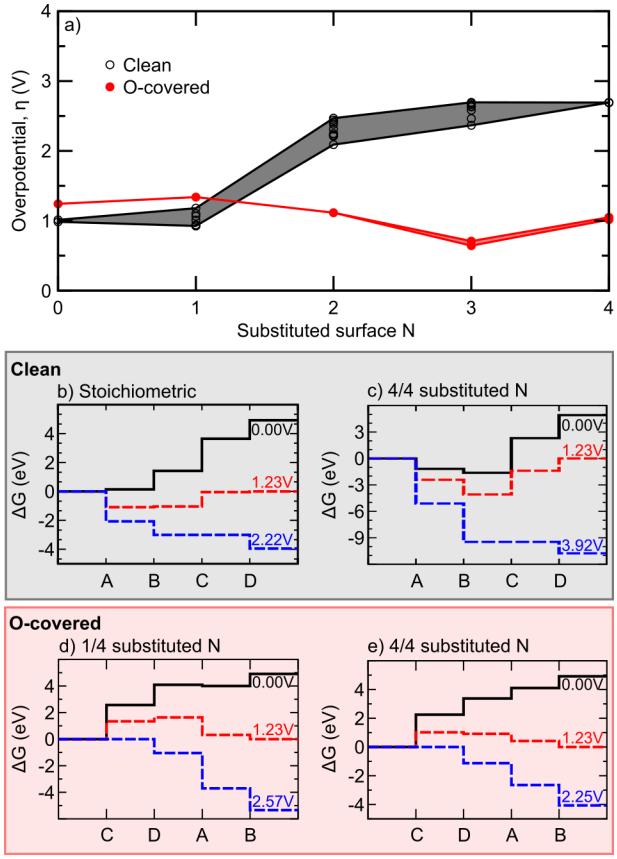

Figure 6: a) Computed overpotentials for the clean and fully O-covered (001) surface as a function of the substitution level. Multiple data points at the same substitution level stand for different active sites. Free energy diagrams at pH 0 on the clean surface in b) its stoichiometric state and c) at full substitution of all surface nitrogen atoms as well as for the O-covered surface d) with one substituted nitrogen and e) full nitrogen substitution.

The potential relevant for photocatalysis is given by the offset between the valence-band maximum and the standard hydrogen electrode. This is computationally challenging to derive[43] but was recently experimentally determined to be 1.45 V[44]. This implies that for all surfaces except the one with four substituted N, the fully O covered state is relevant, whereas for the fully substituted surface the OH covered surface is most relevant. For this reason, we will in the following investigate the OER on the fully O covered surface, which proceeds via the intermediate sequence $*O \rightarrow *OOH \rightarrow * \rightarrow *OH \rightarrow *O$ as well as for the fully substituted surface also for a fully OH covered surface via the intermediate sequence

Table 3: Overpotential determining step (ODS) and overpotential (η) of the most reactive site as a function of the number of substituted N atoms on a surface fully covered with O adsorbates. The ODS letter corresponds to the transition between intermediates given by equations 4-7.

Substituted surface N	Adsorbate	ODS	η (V)
0/4	O	C	1.24
1/4	O	C	1.34
2/4	O	C	1.11
3/4	O	C	0.71
4/4	O	B	1.02
4/4	OH	D	1.45

$*OH \rightarrow *O \rightarrow *OOH \rightarrow * \rightarrow *OH$. As can be seen in Table 3, the overpotential on the fully O covered non-substituted surface is higher than for the clean surface, as also observed for a variety of other perovskite materials[45]. Contrary to the clean surface, we see on the O covered surface, for increasing substitution, initially a small increase in overpotential at 1/4 substitution followed by a substantial drop as also shown in Fig. 6a) before the overpotential increases again for full substitution. This drop in overpotential can be explained with the reduction of the number of O-N dimers on the surface that are not replaced by O-O dimers. These O-N species are extremely stable, requiring a lot of energy to dissociate as required for *OOH formation. The final upturn in overpotential can be related to a change in mechanism, the ODS changing from step C (like for the clean surface) to step B at full substitution of N by O. On the OH covered surface, the overpotential is significantly higher since the possibility to form hydrogen bonds for the OOH intermediate renders the final oxidation and O_2 desorption (step D) the ODS.

The above activity results are summarized in Fig. 7 in form of a volcano plot as function of the descriptor $\Delta G_{\mathrm{O}} - \Delta G_{\mathrm{OH}} = \Delta G_{\mathrm{B}}$. We observe a systematic deviation of the overpotential from the universal scaling relations[31] when the left branch (step C) determines the overpotential. Since on the clean surface, this overestimation is independent of the substitution fraction, we cannot relate it to the formation of O-N dimer species but believe it to be a deviation from the scaling relations as it occurs for roughly one third of materials[31,46,47]. On

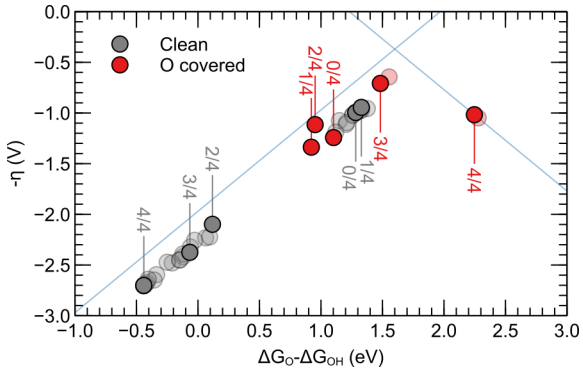

Figure 7: Volcano plot of the negative overpotential as a function of the descriptor $\Delta G_{\mathrm{O}} - \Delta G_{\mathrm{OH}}$ for the clean surface (grey) and the O-covered one (red). The highlighted points correspond to those shown in Tables 2 and 3 and the labels indicate the fraction of substitution. The blue lines show the overpotentials predicted by the universal scaling relations.

the other hand, for the O-covered and fully substituted surface, where the B step determines the overpotential, we find the data points to follow the scaling relations, implying that *OOH binding on the oxynitride may lead to the deviation as it is involved in step C but not step B.

These results imply that the effect of substituting N by O on oxynitride surfaces is more complex than previously reported[19] when considering the full Pourbaix diagram and surfaces other than the clean ones. In particular we find two competing effects on the O-covered surface, which is most relevant under photocatalytic conditions for all but a full substitution of N by O. On one hand, like on the clean surface, substitution of N by O leads to stronger binding of reaction intermediates and a reduced activity. On the other hand, the suppression of O-N dimers due to the reduced number of available surface N atoms leads to an enhanced activity that peaks around 3/4 substitution. Nevertheless strong *OOH binding leads to a deviation from the universal scaling relations and consequently still fairly large overpotentials (0.71 V) even at the ideal substitution level. Moreover, compared to $SrTaO_2N$, $SrNbO_2N$ has surface sites with different oxidation states, leading to a large variability in OER activity.

Conclusion

Our DFT results for $SrNbO_2N$ bulk and its (001) surface show that substitution of N by O is much more likely to occur under OER conditions than for the chemically similar $SrTaO_2N$. We relate this to the multivalent nature of Nb and its more facile reduction. Substitution of N by O on the surface leads to excess charge, which is accommodated on Nb sites, changing their valence from +5 to +4. At substitution levels lower than full substitution, this charge predominantly localizes at specific sites, yielding different OER free energy profiles at different sites on the clean surface. In general we observe a drop of the OER activity (an increase in overpotential) with increasing substitution on the clean surface, which we relate with stronger binding of intermediate species.

Under OER conditions, the surface is however covered with O adsorbates, which on the stoichiometric $SrNbO_2N$ surface slightly increases the overpotential. Upon substitution of more than 1/4 N by O, the overpotential drops considerably, reaching its lowest value at 3/4 substitution. We relate this to two competing effects: the electron injection due to substitution, which increases the binding strength and hence reduces the activity, while a reduction of the number of surface N sites that can form highly stable O-N dimers leads to an enhanced activity. These results show that surface nitrogen loss is not necessarily detrimental to the OER activity but could instead be used to tune the OER activity of perovskite oxynitride photocatalysts.

Acknowledgement

This work was funded by the SNF Professorship Grant PP00P2_157615. Calculations were performed on UBELIX (http://www.id.unibe.ch/hpc), the HPC cluster at the University of Bern and Piz Daint at CSCS under project number s955.

Supporting Information Available

DFT+U test calculations for the density of states.

References

(1) Grätzel, M. Solar Energy Conversion by Dye-Sensitized Photovoltaic Cells. *Inorganic Chemistry* **2005**, *44*, 6841–6851.

(2) Chen, H.; Cong, T. N.; Yang, W.; Tan, C.; Li, Y.; Ding, Y. Progress in Electrical Energy Storage System: A Critical Review. *Progress in Natural Science* **2009**, *19*, 291–312.

(3) Lewis, N. S.; Nocera, D. G. Powering the Planet: Chemical Challenges in Solar Energy Utilization. *PNAS* **2006**, *103*, 15729–15735.

(4) Fujishima, A.; Honda, K. Electrochemical Pphotolysis of Water at a Semiconductor Electrode. *Nature* **1972**, *238*, 37–38.

(5) Khaselev, O.; Turner, J. A. A Monolithic Photovoltaic-Photoelectrochemical Device for Hydrogen Production via Water Splitting. *Science* **1998**, *280*, 425–427.

(6) Rong, X.; Parolin, J.; Kolpak, A. M. A Fundamental Relationship between Reaction Mechanism and Stability in Metal Oxide Catalysts for Oxygen Evolution. *ACS Catalysis* **2016**, *6*, 1153–1158.

(7) Grimaud, A.; Diaz-Morales, O.; Han, B.; Hong, W. T.; Lee, Y.-L.; Giordano, L.; Stoerzinger, K. A.; Koper, M. T. M.; Shao-Horn, Y. Activating Lattice Oxygen Redox Reactions in Metal Oxides to Catalyse Oxygen Evolution. *Nature Chemistry* **2017**, *9*, 457–465.

(8) Yoo, J. S.; Rong, X.; Liu, Y.; Kolpak, A. M. Role of Lattice Oxygen Participation in Understanding Trends in the Oxygen Evolution Reaction on Perovskites. *ACS Catalysis* **2018**, *8*, 4628–4636.

(9) Nørskov, J. K.; Rossmeisl, J.; Logadottir, A.; Lindqvist, L.; Kitchin, J. R.; Bligaard, T.; Jonsson, H. Origin of the Overpotential for Oxygen Reduction at a Fuel-Cell Cathode. *The Journal of Physical Chemistry B* **2004**, *108*, 17886–17892.

(10) Valdés, A.; Qu, Z.-W.; Kroes, G.-J.; Rossmeisl, J.; Nørskov, J. K. Oxidation and Photo-Oxidation of Water on TiO_2 surface. *The Journal of Physical Chemistry C* **2008**, *112*, 9872–9879.

(11) Lin, W.-H.; Cheng, C.; Hu, C.-C.; Teng, H. $NaTaO_3$ Photocatalysts of Different Crystalline Structures for Water Splitting into H_2 and O_2. *Applied Physics Letters* **2006**, *89*, 211904.

(12) Jellison, G. E.; Paulauskas, I.; Boatner, L. A.; Singh, D. J. Optical Functions of $KTaO_3$ as Determined by Spectroscopic Ellipsometry and Comparison with Band Structure Calculations. *Physical Review B* **2006**, *74*, 155130.

(13) Balaz, S.; Porter, S. H.; Woodward, P. M.; Brillson, L. J. Electronic Structure of Tantalum Oxynitride Perovskite Photocatalysts. *Chemistry of Materials* **2013**, *25*, 3337–3343.

(14) Kasahara, A.; Nukumizu, K.; Hitoki, G.; Takata, T.; Kondo, J. N.; Hara, M.; Kobayashi, H.; Domen, K. Photoreactions on $LaTiO_2N$ Under Visible Light Irradiation. *The Journal of Physical Chemistry A* **2002**, *106*, 6750–6753.

(15) Ahmed, M.; Xinxin, G. A Review of Metal Oxynitrides for Photocatalysis. *Inorganic Chemistry Frontiers* **2016**, *3*, 578–590.

(16) Kasahara, A.; Nukumizu, K.; Takata, T.; Kondo, J. N.; Hara, M.; Kobayashi, H.; Domen, K. $LaTiO_2N$ as a Visible-Light (< 600 nm)-Driven Photocatalyst (2). *The Journal of Physical Chemistry B* **2003**, *107*, 791–797.

(17) Maegli, A. E.; Pokrant, S.; Hisatomi, T.; Trottmann, M.; Domen, K.; Weidenkaff, A. Enhancement of Photocatalytic Water Oxidation by the Morphological Control of $LaTiO_2N$ and Cobalt Oxide Catalysts. *The Journal of Physical Chemistry C* **2014**, *118*, 16344–16351.

(18) Yang, M.; Oró-Solé, J.; Rodgers, J. A.; Jorge, A. B.; Fuertes, A.; Attfield, J. P. Anion Order in Perovskite Oxynitrides. *Nature Chemistry* **2011**, *3*, 47–52.

(19) Ouhbi, H.; Aschauer, U. Nitrogen Loss and Oxygen Evolution Reaction Activity of Perovskite Oxynitrides. *ACS Materials Letters* **2019**, *1*, 52–57.

(20) Giannozzi, P.; Baroni, S.; Bonini, N.; Calandra, M.; Car, R.; Cavazzoni, C.; Ceresoli, D.; Chiarotti, G. L.; Cococcioni, M.; Dabo, I. et al. Quantum ESPRESSO: a Modular and Open-Source Software Project for Quantum Simulations of Materials. *Journal of Physics: Condensed Matter* **2009**, *21*, 395502.

(21) Giannozzi, P.; Andreussi, O.; Brumme, T.; Bunau, O.; Nardelli, M. B.; Calandra, M.; Car, R.; Cavazzoni, C.; Ceresoli, D.; Cococcioni, M. et al. Advanced Capabilities for Materials Modelling with Quantum ESPRESSO. *Journal of Physics: Condensed Matter* **2017**, *29*, 465901.

(22) Perdew, J. P.; Burke, K.; Ernzerhof, M. Generalized Gradient Approximation Made Simple. *Physical Review Letters* **1996**, *77*, 3865–3868.

(23) Vanderbilt, D. Soft Self-Consistent Pseudopotentials in a Generalized Eigenvalue Formalism. *Physical Review B* **1990**, *41*, 7892.

(24) Monkhorst, H. J.; Pack, J. D. Special Points for Brillouin-Zone Integrations. *Physical Review B* **1976**, *13*, 5188.

(25) Heyd, J.; Scuseria, G. E.; Ernzerhof, M. Hybrid functionals based on a screened Coulomb potential. *The Journal of Chemical Physics* **2003**, *118*, 8207–8215.

(26) Krukau, A. V.; Vydrov, O. A.; Izmaylov, A. F.; Scuseria, G. E. Influence of the exchange screening parameter on the performance of screened hybrid functionals. *The Journal of Chemical Physics* **2006**, *125*, 224106.

(27) Eglitis, R. I. Comparative First-Principles Calculations of SrTiO3, BaTiO3, PbTiO3 and CaTiO3 (001), (011) and (111) Surfaces. *Ferroelectrics* **2015**, *483*, 53–67.

(28) Ninova, S.; Pokrant, S.; Aschauer, U. Surface Orientation and Structure of LaTiO2N Nanoparticles. *ACS Applied Energy Materials* **2020**, *3*, 5867–5873.

(29) Bengtsson, L. Dipole Correction for Surface Supercell Calculations. *Physical Review B* **1999**, *59*, 12301.

(30) Chase, M. W. *Chapter 1*; NIST-JANAF thermochemical tables; American Chemical Society, 1998.

(31) Man, I. C.; Su, H.-Y.; Calle-Vallejo, F.; Hansen, H. A.; Martínez, J. I.; Inoglu, N. G.; Kitchin, J.; Jaramillo, T. F.; Nørskov, J. K.; Rossmeisl, J. Universality in Oxygen Evolution Electrocatalysis on Oxide Surfaces. *ChemCatChem* **2011**, *3*, 1159–1165.

(32) Gauthier, J. A.; Dickens, C. F.; Heenen, H. H.; Vijay, S.; Ringe, S.; Chan, K. Unified Approach to Implicit and Explicit Solvent Simulations of Electrochemical Reaction Energetics. *Journal of Chemical Theory and Computation* **2019**, *15*, 6895–6906.

(33) Clarke, S. J.; Hardstone, K. A.; Michie, C. W.; Rosseinsky, M. J. High-Temperature Synthesis and Structures of Perovskite and n= 1 Ruddlesden- Popper Tantalum Oxynitrides. *Chemistry of Materials* **2002**, *14*, 2664–2669.

(34) Ebbinghaus, S.; Weidenkaff, A.; Rachel, A.; Reller, A. Powder Neutron Diffraction of $SrNbO_2N$ at Room Temperature and 1.5 K. *Acta Crystallographica Section C* **2004**, *60*, i91–i93.

(35) Ouhbi, H.; Aschauer, U. Water Oxidation Chemistry of Oxynitrides and Oxides: Comparing $NaTaO_3$ and $SrTaO_2N$. *Surface Science* **2018**, *677*, 258–263.

(36) Yang, M.; Oró-Solé, J.; Rodgers, J. A.; Jorge, A. B.; Fuertes, A.; Attfield, J. P. Anion order in perovskite oxynitrides. *Nature Chemistry* **2011**, *3*, 47–52.

(37) Clark, L.; Oró-Solé, J.; Knight, K. S.; Fuertes, A.; Attfield, J. P. Thermally Robust Anion-Chain Order in Oxynitride Perovskites. *Chemistry of Materials* **2013**, *25*, 5004–5011.

(38) Butler, M. A.; Ginley, D. S. Prediction of Flatband Potentials at Semiconductor-Electrolyte Interfaces from Atomic Electronegativities. *Journal of The Electrochemical Society* **1978**, *125*, 228–232.

(39) Xu, Y.; Schoonen, M. A. The absolute energy positions of conduction and valence bands of selected semiconducting minerals. *American Mineralogist* **2000**, *85*, 543–556.

(40) Castelli, I. E.; García-Lastra, J. M.; Hüser, F.; Thygesen, K. S.; Jacobsen, K. W. Stability and bandgaps of layered perovskites for one- and two-photon water splitting. *New Journal of Physics* **2013**, *15*, 105026.

(41) Buckeridge, J.; Scanlon, D. O.; Walsh, A.; Catlow, C. R. A. Automated Procedure to Determine the Thermodynamic Stability of a Material and the Range of Chemical Potentials Necessary for its Formation Relative to Competing Phases and Compounds. *Computer Physics Communications* **2014**, *185*, 330–338.

(42) Bouri, M.; Aschauer, U. Suitability of Different Sr_2TaO_3N Surface Orientations for Photocatalytic Water Oxidation. *Chemistry of Materials* **2020**, *32*, 75–84.

(43) Wu, Y.; Chan, M. K. Y.; Ceder, G. Prediction of Semiconductor Band Edge Positions in Aqueous Environments from First Principles. *Physical Review B* **2011**, *83*, 235301.

(44) Nakamura, T.; Kikuchi, R.; Yamashita, Y.; Kuroda, T.; Chikyow, T.; Kaneko, Y. Evaluation of Band Alignment of $SrNbO_2N$ using Hard X-ray Photoelectron Spectroscopy. *The Journal of Physical Chemistry C* **2020**, *124*, 5528–5532.

(45) Montoya, J. H.; Doyle, A. D.; Nørskov, J. K.; Vojvodic, A. Trends in Adsorption of Electrocatalytic Water Splitting Intermediates on Cubic ABO_3 Oxides. *Phys. Chem. Chem. Phys.* **2018**, *20*, 3813–3818.

(46) Koper, M. T. M. Thermodynamic Theory of Multi-Electron Transfer Reactions: Implications for Electrocatalysis. *Journal of Electroanalytical Chemistry* **2011**, *660*, 254 – 260.

(47) Koper, M. T. M. Theory of Multiple Proton–Electron Transfer Reactions and its Implications for Electrocatalysis. *Chemical Science* **2013**, *4*, 2710–2723.

Graphical TOC Entry